Postprint of: Grubba R., Kaniewska K., Ponikiewski Ł., Cristóvão B., Ferenc W., Dragulescu-Andrasi A., Krzystek J., Stoian S., Pikies J., Synthetic, Structural, and Spectroscopic Characterization of a Novel Family of High-Spin Iron(II) [(β-Diketiminate)(phosphanylphosphido)] Complexes, INORGANIC CHEMISTRY, Vol. 56, No 18 (2017), pp. 11030–11042, DOI: 10.1021/acs.inorgchem.7b01374

Synthetic, Structural, and Spectroscopic Characterization of a Novel Family of High-Spin Iron(II) [(*β*-Diketiminate)(phosphanylphosphido)] Complexes

Rafał Grubba,[†] Kinga Kaniewska,[†] Łukasz Ponikiewski,[†] Beata Cristóvão,[‡] Wiesława Ferenc,[‡] Alina Dragulescu-Andrasi,[§] J. Krzystek,[∥] Sebastian A. Stoian,[§,∥,⊥] and Jerzy Pikies[†]

[†]Department of Inorganic Chemistry, Chemical Faculty, Gdańsk University of Technology, G. Narutowicza St. 11/12, Gdańsk PL-80-233, Poland

[‡]Department of General and Coordination Chemistry, Faculty of Chemistry, Maria Curie-Skłodowska University, Maria Curie-Skłodowska Sq. 2, Lublin PL-20-031, Poland

[§]Department of Chemistry and Biochemistry, Florida State University, Tallahassee, Florida 32306, United States

[∥]National High Magnetic Field Laboratory, Florida State University, Tallahassee, Florida 32310, United States

[⊥]Department of Chemistry, University of Idaho, Moscow, Idaho 83844, United States

ABSTRACT: This work describes a series of iron(II) phosphanylphosphido complexes. These compounds were obtained by reacting lithiated diphosphanes $R_2PP(SiMe_3)Li$ (R = *t*-Bu, *i*-Pr) with an iron(II) *β*-diketiminate complex, $[LFe(\mu_2\text{-}Cl)_2Li(DME)_2]$ (**1**), where DME = 1,2-dimethoxyethane and L = Dippnacnac (*β*-diketiminate). While the reaction of **1** with *t*-$Bu_2PP(SiMe_3)Li$ yields $[LFe(\eta^1\text{-}Me_3SiPP\text{-}t\text{-}Bu_2)]$ (**2**), that of **1** with equimolar amounts of *i*-$Pr_2PP(SiMe_3)Li$, in DME, leads to $[LFe(\eta^2\text{-}i\text{-}Pr_2PPSiMe_3)]$ (**3**). In contrast, the reaction of **1** with $(i\text{-}Pr_2N)_2PP(SiMe_3)Li$ provides not an iron-containing complex but 1-[(diisopropylamino)phosphine]-2,4-bis(diisopropylamino)-3-(trimethylsilyl)tetraphosphetane (**4**). The structures of **2**–**4** were determined using diffractometry. Thus, **2** exhibits a three-coordinate iron site and **3** a four-coordinate iron site. The increase in the coordination number is induced by the change from an anticlinal to a synclinal conformation of the phoshpanylphosphido ligands. The electronic structures of **2** and **3** were assessed through a combined field-dependent ^{57}Fe Mössbauer and high-frequency and -field electron paramagnetic resonance spectroscopic investigation in conjunction with analysis of their magnetic susceptibility and magnetization data. These studies revealed two high-spin iron(II) sites with $S = 2$ ground states that have different properties. While **2** exhibits a zero-field splitting described by a positive D parameter ($D = +17.4$ cm^{-1}; $E/D = 0.11$) for **3**, this parameter is negative [$D = -25(5)$ cm^{-1}; $E/D = 0.15(5)$]. Density functional theory (DFT) and time-dependent DFT (TDDFT) calculations provide insights into the origin of these differences and allow us to rationalize the fine and hyperfine structure parameters of **2** and **3**. Thus, for **2**, the spin–orbit coupling mixes a z^2-type ground state with two low-lying {xz/yz} orbital states. These interactions lead to an easy plane of magnetization, which is essentially parallel to the plane defined by the N–Fe–N atoms. For **3**, we find a yz-type ground state that is strongly mixed with a low-lying z^2-type orbital state. In this case, the spin–orbit interaction leads to a partial unquenching of the orbital momentum along the x axis, that is, to an easy axis of magnetization oriented roughly along the Fe–P bond of the phosphido moiety.

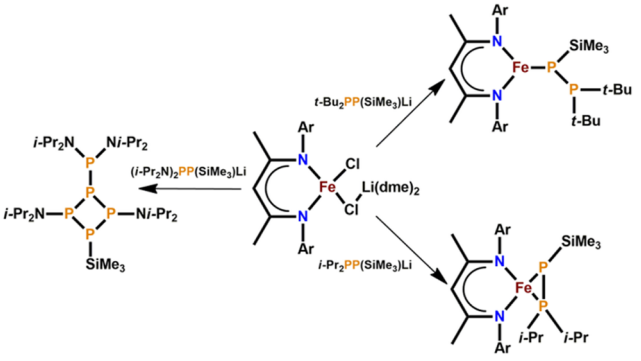

1. INTRODUCTION

Low-coordinate, high-spin iron(II) compounds exhibit fascinating chemical reactivity and unusual electronic structures, highlighting their importance from both a fundamental and a practical perspective. These compounds have attracted increased research interest for their potential as catalysts, as well as for their importance as structural and functional synthetic models of key enzymes, including nitrogenases and hydrogenases.[1,2] Heteroleptic, three- and four-coordinate iron(II) complexes have been successfully stabilized by employing sterically encumbered *β*-diketiminate (Dippnacnac) ligands.[3,4] For some of these compounds, detailed field-dependent ^{57}Fe Mössbauer and X-band electron paramagnetic resonance (EPR) spectroscopic studies have revealed the presence of large unquenched orbital momenta originating

from the strong spin−orbit coupling acting on quasi-degenerate orbital ground states.[5] Consequently, such compounds show an increased potential for exhibiting single-molecule-magnet-like behavior.[6]

Phosphido ligands can be considered as heavier congeners of amido groups. The essential difference between them lies in the stronger propensity of the phosphido to function as a bridging ligand. This dissimilarity arises from the stronger π-donor ability of amido ligands[7] and the steric demands of phosphido groups.[8] It was shown that, in terms of the structure and stability, the $P(SiPh_3)_2$ moiety closely resembles the $N(SiMe_3)_2$ group.[9] In the early 1980s, Schäfer reported the formation of an iron-based complex, $[Cp(CO)_2FeP(SiMe_3)_2]$, enclosing a terminal phosphido ligand, via $[Cp(CO)_2FeCl]$ and $LiP(SiMe_3)_2$ metathesis.[10] In a related complex $[Cp(CO)_2FeP(CF_3)_2]$, the phosphorus-based ligand, $P(CF_3)_2$, adopts a terminal geometry as well.[11] Unlike the $P(SiMe_3)_2$ and $P(CF_3)_2$ moieties, t-Bu_2P and smaller phosphido ligands adopt a bridging geometry upon coordination of the iron centers. Thus, $[Cp(CO)_2FeCl]$ reacts with $PhP(SiMe_3)_2$, yielding $[Cp(CO)_2Fe\{\mu_2\text{-}PPh(SiMe_3)\}]_2$.[12] Similarly, $[(Me_3P)_2FeCl_2]$ reacts with t-Bu_2PLi, yielding $[(Me_3P)FeCl(\mu_2\text{-}P\text{-}t\text{-}Bu_2)]_2$.[13]

There are only a few other reports of iron β-diketiminate complexes incorporating phosphorus-donor coligands. One example is the $LFe^{I}PPh_3$ complex bearing a phosphine ligand, which was obtained by reacting the dinitrogen complex LFeNNFeL [L = DippNC(Me)CHC(Me)NDipp] with PPh_3.[14] Stephan et al. described the reaction of the iron(I) β-diketiminate compound, $[LFe(\eta^2\text{-}CH_2CPh_2)]$ [L = DippNC(Me)CHC(Me)NDipp], with primary and secondary phosphines, Ph_2PH or $PhPH_2$, that resulted in P−H and P−C bond activation with the formation of phosphinidene-incorporating iron(III) dimers, $[LFe(\mu\text{-}PPh)]_2$.[15] Alternative routes to iron β-diketiminate complexes supported by phosphorus-based ligands were presented by Driess et al.[16] and Scheer et al.[17] The reaction under mild conditions of an iron β-diketiminate complex, [LFe(toluene)] (L = $DippNC_3H_3NDipp$), with white phosphorus furnished a dinuclear iron(III) complex, $[(LFe)_2(\mu\text{-}\eta^2\text{:}\eta^2\text{-}P_2)_2]$, featuring two bridging $[P_2]^{2-}$ ligands.[16] The reduction of $[(LFe)_2(\mu\text{-}\eta^2\text{:}\eta^2\text{-}P_2)_2]$ with potassium metal resulted in the formation of a mixed-valent iron(II,III) complex, which is isostructural with its neutral precursor.[16] The reactivity of [LFe(toluene)] toward P_4 was found to be sensitive to minor alterations of the β-diketiminate ligands.[17] Thus, the steric properties of nacnac ligands exert a profound influence on the final iron(II) complex formed, which include $[P_8]^{4-}$ or *cyclo*-$[P_4]^{2-}$ structural motifs for β-diketiminate ligands dmpNC(Me)CHC(Me)Ndmp and DippNC(Me)CHC(Me)NDipp, respectively.[17] Recently, iron β-diketiminate complexes, $[LFe(CH_2SiMe_3)]$ [L = dmpNC(Me)CHC(Me)Ndmp and DippNC(Me)CHC(Me)NDipp], were used as effective pre-catalysts in the dehydrocoupling of primary and secondary phosphines[18] and in the hydrophosphination of alkenes.[18,19] The phosphido complexes of iron, $[LFe(PR_2)]$ and $[LFe(PRH)]$, were postulated to be active catalysts in these transformations. More recently, β-diketiminate phoshido complexes were found to play a crucial role in the hydrophosphination of nonactivated unsaturated C−C bonds.[19] Utilization of the β-diketiminate complex $[LFe(CH_2SiMe_3)]$ as a precatalyst in the cyclization of primary phosphines led to the isolation of a dimeric phosphido complex, $[LFe(PRH(CH_2)_3CH{=}CH_2]_2$ [L = DippNC(Me)CHC(Me)NDipp], as a catalytic intermediate.[19] Thus, in the light of recent reports, it is worth emphasizing the need for further studies of β-diketiminate iron complexes with phosphido coligands to expand this important class of iron complexes and their application as effective catalysts.

We have recently reported the synthesis and reactivity of several low-valent phosphorus-based compounds, in particular of nucleophilic phosphanylphosphinidene complexes (R_2PP) and phosphanylphosphido complexes ($R_2PPSiMe_3$).[20−32] The diphosphorus counterparts of the complexes with R_2P and RP ligands have been explored to a much lesser extent. Up to now, only a few examples of titanium,[27] zirconium,[22,26] and hafnium[23] complexes having $R_2PPSiMe_3$ ligands have been isolated. In this study, we describe a novel class of β-diketiminate-supported high-spin ferrous complexes that incorporate phosphanylphosphido coligands. The structural and spectroscopic characterization of these compounds revealed that their electronic structures and magnetic properties are tightly coupled to conformation of the phosphanylphosphido moieties. The change from an anticlinal to a synclinal conformation of the $R_2PPSiMe_3$ moiety leads not only to an increase in the coordination number (CN) but also to a change in the nature of the electronic ground state and the character of spin−orbit interactions. Thus, the four-coordinate complex **3** exhibits an overall behavior that is rather similar to those observed for analogous low-coordinate, iron(II) β-diketiminate complexes, in particular, of $[LFe(\mu_2\text{-}Cl)_2Li(THF)_2]$ (THF = tetrahydrofuran).[33] In contrast, the properties of the three-coordinate iron complex **2** are similar not with those of analogous iron(II) β-diketiminate complexes but rather with those of homoleptic, planar-trigonal iron(II) sulfides, $[Fe^{II}(SR)_3]^-$ (R = C_6H_2-2,4,6-t-Bu_3).[34,35] Our computational investigation and theoretical analysis of the fine and hyperfine structures of **2** and **3** provides a clear rational for these observations vide infra.

2. METHODS AND MATERIALS

2.1. Synthesis. The 1,2-dimethoxyethane (DME) solvent was dried over potassium/benzophenone and distilled under argon. Pentane was dried over sodium/benzophenone/diglyme and distilled under argon. All manipulations were performed in flame-dried Schlenk-type glassware on a vacuum line or in an argon-filled glovebox. $^{31}P\{^1H\}$ NMR (external standard 85% H_3PO_4) and ^1H NMR (internal standard tetramethylsilane) spectra were recorded on Bruker AV300 MHz, Bruker AV400 MHz, and Varian Unity 500 MHz spectrometers at room temperature. Literature methods were used to prepare $R_2PP(SiMe_3)Li{\cdot}n$THF[36] and $[(Dippnacnac)FeCl_2Li(DME)_2]$ (**1**).[37] All synthesized compounds are extremely moisture- and air-sensitive.

*Synthesis of [(Dippnacnac)Fe(η^1-Me$_3$SiPP-t-Bu$_2$)] (**2**).* A solution of t-$Bu_2PP(SiMe_3)Li{\cdot}2.2$THF (0.207 g, 0.500 mmol) in DME (2.5 mL) was slowly added to **1** (0.366 g, 0.500 mmol) in DME (2 mL) at −30 °C. The temperature of the reaction was maintained between −30 and −20 °C for 0.5 h. After warming to room temperature, the solvent was evaporated under vacuum. The residue was extracted with pentane (10 mL), and LiCl was filtered off. The filtrate was concentrated to 3.5 mL and stored at +4 and −20 °C. After a few days, dark-red crystals of **2** were formed (0.127 g, 0.176 mmol; yield 35%).

Anal. Calcd for $C_{40}H_{68}FeN_2P_2Si$: C, 66.46; H, 9.48; N, 3.88. Found: C, 65.94; H, 9.51; N, 3.87.

^1H NMR (400 MHz, toluene-d_8, 25 °C): 97.59 (CH nacnac, 1H), 10.03 (Me nacnac, 6H), 7.88 ($SiMe_3$, 9H), 7.14 (*m*-H, 4H), 3.08 (*t*-Bu, 18H), 2.35 (*i*-Pr methyl, 6H), 1.19 (*i*-Pr methyl, 6H), 0.33 (*p*-H, 2H), −16.75 (*i*-Pr methyl, 6H), −33.39 (*i*-Pr methyl, 6H), −39.37 (*i*-Pr methine, 1H), −43.61 (*i*-Pr methine, 1H), −66.13 (*i*-Pr methine, 2H).

*Synthesis of [(Dippnacnac)Fe(η^2-i-Pr$_2$PPSiMe$_3$)] (**3**).* A solution of *i*-Pr$_2$PP(SiMe$_3$)Li·3THF (0.222 g, 0.500 mmol) in DME (2.5 mL) was slowly added to **1** (0.366 g, 0.500 mmol) in DME (2 mL) at −30 °C. The temperature of the reaction was maintained between −30 and −20 °C for 0.5 h. After warming to room temperature, the solvent was evaporated under vacuum. Then the residue was extracted with pentane (10 mL), and LiCl was filtered off. The filtrate was concentrated to 3.5 mL, and a dark precipitate was separated after storage at +4 °C overnight. The resulting clear solution was further stored at −20 °C. After a few days, bright-red crystals of **3** were deposited (0.183 g, 0.263 mmol; yield 53%).

Anal. Calcd for $C_{38}H_{65}N_2P_2SiFe$: C, 65.59; H, 9.42; N, 4.03. Found: C, 65.31; H, 9.23; N, 3.89.

^{1}H NMR (400 MHz, toluene-d_8, 25 °C): 122.38 (CH nacnac, 1H), 44.95 (SiMe$_3$, 9H), 23.17 (Me nacnac, 6H), 8.19 (*m*-H, 4H), 5.09 (*i*-Pr$_2$P methyl, 6H), 0.72 (*i*-Pr methyl, 12H), 0.34 (*p*-H, 2H), −13.67 (*i*-Pr$_2$P methyl, 6H), −38.16 (*i*-Pr methyl, 12H), −43.70 (*i*-Pr methine, 2H), −59.93 (*i*-Pr methine, 2H). The signals of the methine protons of the *i*-Pr$_2$P groups are not observed because of their proximity to the metal center.

*Synthesis of 1-[(Diisopropylamino)phosphine]-2,4-bis-(diisopropylamino)-3-(trimethylsilyl)tetraphosphetane (**4**).* A solution of (*i*-Pr$_2$N)$_2$PP(SiMe$_3$)Li·1.5THF (0.450 g; 1.00 mmol) in DME (2.5 mL) was slowly added to **1** (0.320 g, 0.440 mmol) in DME (2 mL) at −30 °C. After warming to room temperature, the solution was concentrated to 3.5 mL and stored at −30 °C. After a few days, colorless crystals of **4** were deposited (0.230 g, 0.366 mmol; yield 91%).

^{1}H NMR (see Scheme 1 for atom labeling): 3.96 (br m, *i*-Pr methine, 2H), 3.96 (br m, *i*-Pr methine, 2H), 3.62 (hpt, 6.4 Hz, *i*-Pr methine, 2H), 3.59 (hpt, 6.4 Hz, *i*-Pr methine, 2H), 1.37 (m, (*i*-Pr methyl, 12H), 1.26 (m, *i*-Pr methyl, 12H), 0.60 (d, 3.37 Hz, PSiMe$_3$, 9H). ^{31}P{^{1}H} NMR (spin system AEM$_2$X): 62.65 (A, (*i*-Pr$_2$N)$_2$P, m), 8.50 (E, P (unsubstituted), m), −20.55 (M, *i*-Pr$_2$NP, m), −84.74 (X, Me$_3$SiP, m). $^1J_{EM}$ = −169. 85 Hz, $^2J_{EX}$ = 36.86 Hz, $^1J_{AE}$ = −185.58 Hz, $^1J_{MX}$ = −177.51 Hz, $^2J_{AM}$ = 192.59 Hz, and $^3J_{AX}$ = 25.78 Hz. ^{31}P{^{1}H} NMR inspection of the reaction solution: 81.5 (s, (*i*-Pr$_2$N)$_2$PP(N*i*-Pr$_2$)$_2$), 59.84 (s, unknown compound), −254.0 (s, P(SiMe$_3$)$_3$).

Scheme 1. Structure of the Tetraphosphetane 4

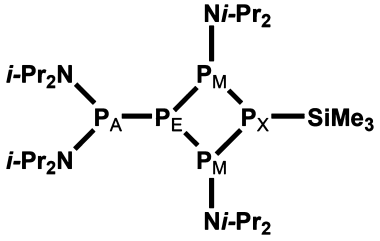

2.2. X-ray Crystallography. X-ray-quality single crystals of **2**−**4** were selected for the X-ray diffraction experiments at 150 K. Diffraction data of **4** were collected on a diffractometer equipped with a STOE IPDS 2 imaging-plate detector system using Mo Kα radiation with a graphite monochromator (λ = 0.71073 Å). The diffraction intensities of **2** and **3** were collected on a Stadi Vari diffractometer equipment with a Pilatus 300K detector with a graphite monochromator (λ = 1.54186 Å for **2**; λ = 0.71073 Å for **3**). The structures were solved by direct methods and refined against F^2 least-squares techniques using the *SHELXS-97* and *SHELXL-97* programs.[38] Non-hydrogen atoms were refined with anisotropic displacement parameters; hydrogen atoms were usually refined using the isotropic model with U_{iso}(H) values fixed as 1.5U_{eq} of carbon atoms for −CH$_3$ groups or 1.2U_{eq} for −CH groups and aromatic H atoms.

2.3. Mössbauer Spectroscopy. Samples of **2** and **3** investigated by ^{57}Fe Mössbauer spectroscopy contained unenriched, natural-abundance iron. For each complex, about 80 mg polycrystalline powder samples were shipped from Gdańsk, Poland, to Tallahassee, FL, in sealed Schlenk flasks. These flasks were opened in an argon-filled glovebox ([O_2(g)] < 1 ppm), where the crystalline material was transferred into custom-made Delrin cups appropriately designed for Mössbauer (∼30 mg) and for high-frequency and -field EPR (HFEPR; ∼50 mg) measurements. Subsequently, the sample cups were stored and handled under LN_2. Variable-field, variable-temperature spectra were recorded using a constant-acceleration spectrometer. The spectrometer was fitted with a flow-type Janis Super-Varitemp 8DT cryostat that was cooled with liquid helium and equipped with an 8 T superconducting magnet. This setup allowed for the generation of magnetic fields parallel to the 14.4 keV γ-radiation used to observe the Mössbauer effect. The source consisted of 100 mCi ^{57}Co dispersed in rhodium foil and was incorporated in a vertical velocity transducer system. The 4.2 K spectra were recorded, while the sample space of the cryostat was flooded with liquid helium. Variable-temperature spectra were recorded in a flow of helium gas that was controlled using a needle-type valve. The sample temperature was determined using a Cernox sensor and maintained using a 50 Ω heater powered by a Cryocon 32B temperature controller. The isomer shifts are reported against the centroid of a spectrum of α-iron metal foil recorded at room temperature. The spectra were analyzed in the framework of a standard S = 2 spin Hamiltonian, as implemented by the *SpinHam* option of the *WMOSS* spectral analysis software (formerly Web Research Co., Edina, MN).[39]

2.4. HFEPR. HFEPR measurements were carried out on a custom-built spectrometer that was previously described.[40] However, in this case, microwaves of the desired frequency were obtained using a subterahertz wave generator from Virginia Diodes operating at 13 ± 1 GHz and equipped with a cascade of frequency multipliers. HFEPR spectra were interpreted in terms of a standard spin Hamiltonian for S = 2 and simulated using the program *SPIN* (from A. Ozarowski).

2.5. Magnetometry. Magnetic susceptibilities for polycrystalline samples of **2** and **3** were measured over the temperature range from 1.8 to 300 K at a magnetic field of 0.1 T using a Quantum Design SQUID-VSM magnetometer. Field dependencies of magnetization were measured in the 2−6 K range in applied fields of up to 7 T. The obtained data were corrected for the sample-holder signal and for diamagnetism using Pascal's constants.[41] While fits of the susceptibility data were obtained using the *JulX* program written by Prof. Eckhard Bill, the reduced magnetization data were simulated using an in-house-developed program.[42]

2.6. Density Functional Theory (DFT) Calculations. The DFT calculations were performed using the *Gaussian09* (revisions A02 and C01) suite of quantum-chemical programs and the B3LYP/6-311G, B3LYP/6-311++G*, and BPW91/cc-pvtz functional/basis set combinations.[43] Self-consistent-field (SCF) and geometry optimizations were performed using tight and default convergence criteria, respectively. The stability of the ground state was assessed on the basis of time-dependent SCF calculations and used as the reference state when all single-electron excitations were found to be positive. Population analyses were performed using Mulliken population analysis and natural population analysis (NPA), as implemented in the *NBOpro v.6* program suite.[44] The predicted ΔE_Q and η values describing the electric-field gradient (EFG) and the predicted ^{57}Fe hyperfine coupling constants were estimated using the standard *prop* keyword of the Gaussian code. The predicted isomer shift values were determined using the calibration given by Vrajmasu et al.[45] The potential energy change as a function of a given structural parameter was evaluated by performing a series of relaxed scans for which one internal coordinate was kept fixed and all others were optimized. Finally, the van der Waals volume and the perimeter of selected substituents were calculated considering the volume encompassed by the electron density isosurface with a value of 0.001 e/bohr^3 using the *Multiwfn* software.[46]

3. RESULTS

3.1. Synthesis and Reactivity. The series of phosphanylphosphidoiron complexes were synthesized via reactions of R$_2$PP(SiMe$_3$)Li (R = *t*-Bu, *i*-Pr) with the iron(II) β-diketiminate complex [LFeCl$_2$Li(DME)$_2$] (**1**), where L =

Scheme 2. Synthesis of the Terminal Phosphanylphosphido Complex 2

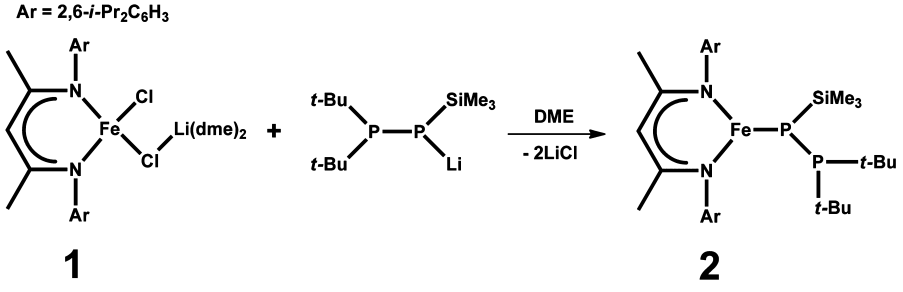

Scheme 3. Synthesis of the Side-On Phosphanylphosphido Complex 3

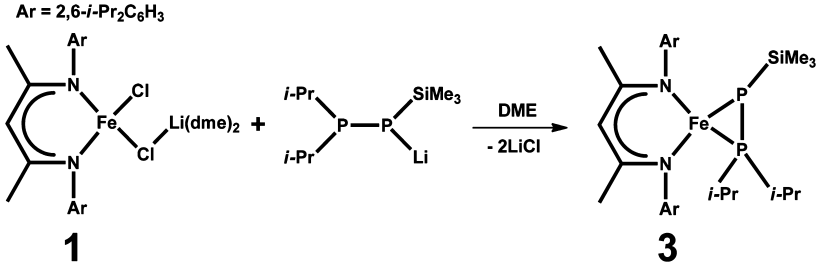

Scheme 4. Synthesis of Tetraphosphetane 4

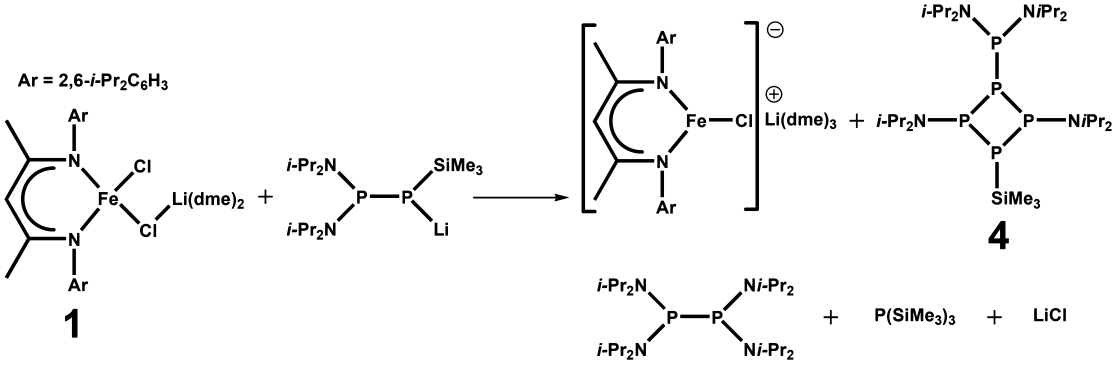

Dippnacnac. Treatment of a DME solution of **1** with an equimolar amount of t-$Bu_2PP(SiMe_3)Li$ yielded a terminal phosphanylphosphido complex, $[LFe(\eta^1\text{-}Me_3SiPP\text{-}t\text{-}Bu_2)]$ (**2**; Scheme 2). Complex **2** was isolated as dark-red crystals from crystallization in pentane at +4 °C (yield 35%). This compound is thermally stable and can be stored under argon at room temperature for a long time.

We studied the influence of steric effects exerted by the R group of diphosphane on the structure of the products. We found that the sterically less demanding precursor i-$Pr_2PP(SiMe_3)Li$ reacts with **1**, yielding $[LFe(\eta^2\text{-}i\text{-}Pr_2PPSiMe_3)]$ (**3**), featuring a side-on-bonded i-$Pr_2PPSiMe_3$ moiety (Scheme 3). Complex **3** formed bright-red crystals and was isolated in a manner similar to that used for compound **2**; however, compared to **2**, the yield is significantly higher (53%). Complex **3** is stable at room temperature but easily reacts with moisture and oxygen.

It is worth emphasizing that, in solvents such as THF and DME, complex **1** does not react with lithium derivatives of diphosphanes to yield phosphanylphosphinidene (R_2PP)-supported iron complexes. In contrast, we observed the formation of such compounds in reactions with platinum, zirconium, molybdenum, and tungsten dichloride complexes when the $SiMe_3$ group of the phosphanylphosphido complex was lithiated by 1 equiv of $R_2PP(SiMe_3)Li$ with subsequent elimination of LiCl and $R_2PP(SiMe_3)_2$.[21−31] Unlike for these results, complexes **2** and **3** show no tendency for lithiation of the $SiMe_3$ group and to form related anionic phosphinidene complexes.

Reactions of **1** with the lithium salt of diphosphane-containing diisopropylamino substituents led to the formation of polyphosphorus compounds. The mixing of DME solutions of **1** with ca. 2-fold molar excess of $(i\text{-}Pr_2N)_2PP(SiMe_3)Li\cdot 1.5THF$ in DME at −30 °C produced dark-brown solutions, which yielded colorless crystals of 1-[(diisopropylamino)-phosphine]-2,4-bis(diisopropylamino)-3-(trimethylsilyl)-tetraphosphetane (**4**), after workup at ambient temperature. Presumably the starting iron(II) complex is reduced to an iron(I) species by the lithium salt of diphosphane with the simultaneous formation of polyphosphorous compounds (Scheme 4). NMR examination of the reaction mixture revealed the formation of tetraphosphetane **4**, $(i\text{-}Pr_2N)_2PP(Ni\text{-}Pr_2)_2$, and $P(SiMe_3)_3$ in a 1:2:4 ratio. Consideration of $(i\text{-}Pr_2N)_2PP(Ni\text{-}Pr_2)_2$ as a product of a reaction leading to **4** is however doubtful. This compound is often present in reactions involving $(i\text{-}Pr_2N)_2PP(SiMe_3)Li$, most likely because of the relatively high stability of the $(i\text{-}Pr_2N)_2P$ radical.

Compound **4** was first reported as a minor, not isolated, reaction product of $(i\text{-Pr}_2\text{N})_2\text{PP(SiMe}_3\text{)Li}$ with $[\text{Cp}_2\text{ZrCl}_2]$. In this case, the main reaction product was 1,3-bis(trimethylsilyl)-2,4-bis(diisopropylamino)tetraphosphetane.[22] The THF solution of $(i\text{-Pr}_2\text{N})_2\text{PP(SiMe}_3\text{)Li}$ is not very stable, and after prolonged storage at ambient temperature, it converts to **4** and $\text{P(SiMe}_3\text{)}_2\text{Li}$.

3.2. X-ray Crystallography. *3.2.1. Crystal Structure of 2.* Complex **2** crystallizes in the $P2_1/c$ space group. The representation of its X-ray structure is shown in Figure 1. In this coordinatively unsaturated compound (12e), the iron atom exhibits a planar, trigonal coordination environment (ΣFe 359.34°). Furthermore, the phosphido atom P1 is also nearly planar (ΣP1 354.03°). The planes defined by N1−Fe1−N2 and Si1−P1−P2 are nearly orthogonal to each other. The geometry at the phosphanyl P2 atom is pyramidal (ΣP2 318.8°). The bite angle N1−Fe1−N2 of 94.57° and the N−Fe bond lengths are typical of three-coordinate iron diketiminate compounds.[3] The Fe1−P1 distance of 2.3144(17) Å is long and has a clear single-bond character.[47] One striking structural feature of **2** is embodied by the short P1−P2 distance of 2.168(2) Å, suggesting a partial double-bond character of the P−P bond. Similar bond lengths were previously linked by us to η^2-coordination mode of the $t\text{-Bu}_2\text{P}{=}\text{PP-}t\text{-Bu}_2$ moiety in $[(\eta^2\text{-R}_2\text{P}{=}\text{PPR}_2)\text{M(Cl)L}]$ (2.12−2.16 Å; L = tertiary phosphine; M = Ni, Pd, Pt)[48] and in $[(\eta^2\text{-}t\text{-Bu}_2\text{P}{=}\text{PP-}t\text{-Bu}_2)\text{M}(2,6\text{-}i\text{-Pr}_2\text{C}_6\text{H}_3\text{N})_2\text{Cl}]$ (2.15−2.16 Å; M = Mo, W).[49] We have discussed the geometries of these nonclassical phosphido ligands in terms of a η^2-bonded diphosphenium cation.[48]

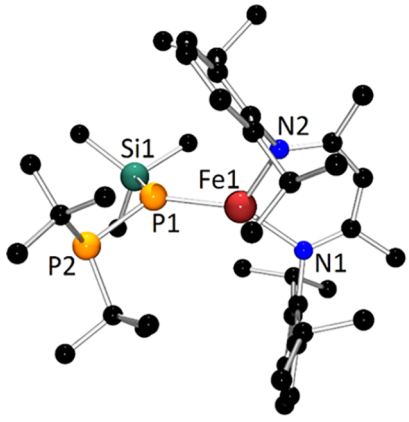

Figure 1. Molecular structure of **2** showing the atom numbering scheme. Hydrogen atoms have been omitted for clarity. Selected bond lengths (Å) and bond angles (deg) for **2**: Fe1−N1 1.999(4), Fe1−N2 1.987(4), Fe1−P1 2.3144(17), P1−P2 2.168(2); N1−Fe1−N2 94.57(18), N1−Fe1−P1 124.27(13), N2−Fe1−P1 140.50(15), Fe1−P1−P2 127.40(10).

3.2.2. Crystal Structure of 3. Compound **3** crystallizes in the $P\bar{1}$ space group. The ORTEP diagram of complex **3** is shown in Figure 2. The Fe1 atom displays a distorted tetrahedral geometry. The planes defined by N1−Fe1−N2 and Fe1−P1−P2 are nearly perpendicular to each other. The phosphanyl P2 atom exhibits a pyramidal geometry (ΣP2 318.8°). The bite angle N1−Fe1−N2 of 93.02° and the N−Fe bond lengths are typical for three-coordinate iron diketiminate compounds.[3] While the Fe1−P1 distance of 2.3638(9) Å is long and almost the same as that in **2**, the distance Fe1−P2 of 2.5070(10) Å is substantially longer. Thus, the bonding of $i\text{-Pr}_2\text{PPSiMe}_3$ to the iron center adopts an intermediate mode between terminal and side-on. The P1−P2 distance of 2.1490(10) Å is shorter than that in **2** and clearly indicates a partial double-bond character. Thus, the side-on bonding of a $\text{R}_2\text{PPSiMe}_3$ ligand clearly enhanced the multiple-bond character of the P−P bond.

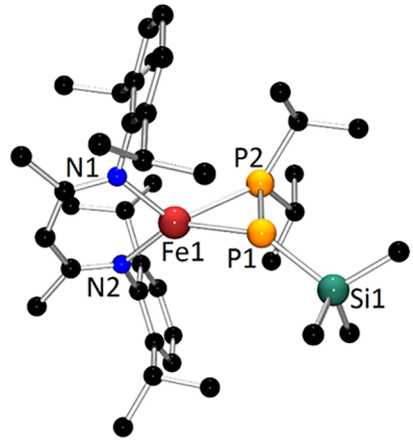

Figure 2. Molecular structure of **3** showing the atom numbering scheme. Hydrogen atoms have been omitted for clarity. Selected bond lengths (Å) and bond angles (deg) for **3**: Fe1−N1 2.003(2), Fe1−N2 2.0218(19), Fe1−P1 2.3638(9), Fe1−P2 2.5070(10), P1−P2 2.1490(10); N1−Fe1−N2 93.02(8), P1−Fe1−P2 52.26(3), Fe1−P1−P2 67.30(4).

Our recent investigation of the phosphanylphosphido complexes supported by transition-metal ions suggests that coligands such as the cyclopentadienyl anion in the case of early transition metals stabilize terminal coordination of the $\text{R}_2\text{PPSiMe}_3$ ligand to the metal center,[22,23] whereas nitrogen ligands like imido or nacnac stabilize side-on coordination mode.[26,27,29] To our surprise, the phosphido ligand $t\text{-Bu}_2\text{PPSiMe}_3$ adopts in **2** a terminal geometry, although the similar $i\text{-Pr}_2\text{PPSiMe}_3$ moiety adopts the expected side-on coordination in sterically less demanding **3**.

3.2.3. Crystal Structure of 4. The ORTEP diagram of complex **4**, which crystallizes in the $P\bar{1}$ space group, is shown in Figure 3. The P−P distances in **4** are typical for single P−P

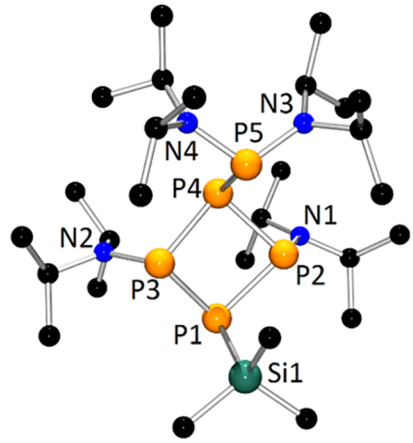

Figure 3. Molecular structure of **4** showing the atom numbering scheme. Hydrogen atoms have been omitted for clarity. Selected bond lengths (Å) and bond angles (deg) for **4**: P1−P2 2.2353(7), P1−P3 2.2446(7), P2−P4 2.2336(7), P3−P4 2.2294(7), P4−P5 2.2460(6); P2−P1−P3 89.82(2), P4−P3−P1 87.02(2), P2−P4−P3 90.28(2), P2−P4−P5 97.97(2).

bonds and for amino-substituted phosphetanes.[50] The P1−P2−P3−P4 ring is folded along the P2−P4 vector (Θ = 19.75°). The nitrogen atoms of the $(i\text{-Pr}_2\text{N})_2\text{P}$ group display exact planar geometry, with nitrogen atoms connected to ring phosphorus atoms being almost planar.

3.3. ^{1}H NMR Studies and Stability in Solution. The stabilities of **2** and **3** in solution were investigated by variable-temperature ^{1}H NMR spectroscopy. Samples were made by dissolving crystals of complexes in toluene-d_8 at −50 °C under an argon atmosphere and then heated to room temperature inside the spectrometer. ^{1}H NMR spectra were recorded in heating mode at −50, −25, 0, and +25 °C. Both complexes exhibit resonances in a very wide range, from 97.59 to −66.13 ppm for **2** and from 122.38 to −59.93 ppm for **3** (see the experimental part for a complete list of resonances). This wide range of ^{1}H NMR resonances is characteristic of paramagnetic, low-valent, iron(II) β-diketiminate complexes.[1] Compound **3** seems to be stable over the range of temperatures from −50 to +25 °C, with only shifts of the signals due to temperature changes being observed. Complex **2** is less stable in a toluene-d_8 solution compared to compound **3**. The ^{1}H NMR spectrum of **2** recorded at +25 °C consists of not only relatively sharp signals from **2** but also very broad signals, which can be attributed to a newly formed iron(III) species. These findings suggest partial disproportionation of **2** in a toluene-d_8 solution at room temperature with the formation of iron(III) and iron(I) complexes. Compound **3** contains a Fe1−P1−P2 ring due to additional coordination of the phosphanyl $i\text{-Pr}_2\text{P}$ group to the metal center, a structural feature that most likely contributes to the increased stability of **3** in the solution compared to **2**.

3.4. ^{57}Fe Mössbauer Spectroscopy. The electronic structures of **2** and **3** were determined, in part, by recording a series of field- and temperature-dependent ^{57}Fe Mössbauer spectra on polycrystalline samples for temperatures between 4.2 and 220 K in applied fields of up to 8 T. The spectra were analyzed in the framework of a typical $S = 2$ spin Hamiltonian described by eqs 1a−1c.[51] The quantities included in these equations have their conventional meanings and are detailed in the Supporting Information.

$$\hat{H} = D\left\{\hat{S}_z^{\,2} - 2 + \frac{E}{D}(\hat{S}_x^{\,2} - \hat{S}_y^{\,2})\right\} + \beta_e \hat{\mathbf{S}}\cdot\tilde{\mathbf{g}}\cdot\vec{\mathbf{B}} + \hat{\mathbf{S}}\cdot\tilde{\mathbf{A}}\cdot\hat{\mathbf{I}} - \beta_n g_n \hat{\mathbf{I}}\cdot\vec{\mathbf{B}} + \delta + \hat{H}_Q \quad (1a)$$

$$\hat{H}_Q = \frac{eQV_{ZZ}}{12}\left[3\hat{I}_Z^{\,2} - \frac{15}{4} + \eta(\hat{I}_X^{\,2} - \hat{I}_Y^{\,2})\right] \quad (1b)$$

$$\Delta E_Q = (eQV_{ZZ}/2)\sqrt{1 + \eta^2/3} \quad (1c)$$

At 4.2 K, the zero-field spectrum of **2** consists of a well-defined, slightly asymmetric quadrupole doublet characterized by an isomer shift $\delta = 0.55(1)$ mm/s, a quadrupole splitting $\Delta E_Q = 1.48(1)$ mm/s, and relatively narrow line widths $\Gamma_{L/R} = 0.31/0.37$ mm/s (Figure 4, left). This doublet accounts for more than 97% of the spectral area, which demonstrates that the sample under investigation was virtually free of impurities. The asymmetry of the quadrupole doublets originates, most likely, from the partial alignment of the polycrystalline material. Figure S3 and Table S2 show that the quadrupole splitting is temperature-independent and, as expected, the second-order Doppler shift induces only a slight change in the isomer shift such that $\delta = 0.50(1)$ mm/s and $\Delta E_Q = 1.49(2)$ mm/s at 180 K. Both the isomer shift and quadrupole splitting of **2** are within the range of values observed for previously characterized high-spin iron(II) complexes that are supported by β-diketimiate ligands (Table 1). The zero-field, 4.2 K spectrum of **3** consists of a well-defined, symmetric quadrupole doublet characterized by $\delta = 0.82$ mm/s, $\Delta E_Q = 1.80$ mm/s, and $\Gamma = 0.37$ mm/s (Figure 4, right). Furthermore, this doublet accounts for essentially all of the iron present in the sample. As the temperature is raised, the quadrupole splitting and the isomer shift exhibit only a minor decrease in their values such that at 180 K $\delta = 0.76$ mm/s and $\Delta E_Q = 1.70$ mm/s (Figure S6 and Table S2). These values are typical of a high-spin iron(II) ion and clearly demonstrate a 2+ oxidation state and high-spin electronic configuration of the metal site.

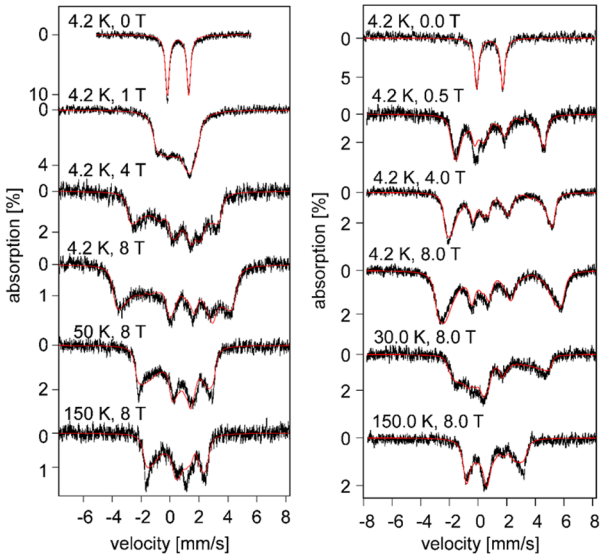

Figure 4. Field- and temperature-dependent ^{57}Fe Mössbauer spectra recorded for polycrystalline samples of **2** (left) and **3** (right). The solid red lines are simulations obtained using the spin Hamiltonian of eq 1 and the parameters listed in Table 1.

Inspection of Figures 4 (left) and S5 shows that for **2** the applied magnetic field leads to the progressive development of a magnetic hyperfine splitting pattern. At 4.2 K, the extent of the observed splitting fails to reach a saturation value even at 8.0 T. This behavior suggests that **2** exhibits a zero-field splitting (ZFS) of the electronic spin sublevels characterized by a relatively large and positive D parameter. These observations were corroborated by the spectral simulations of the complete data set (see the Supporting Information). In particular, analysis of the 4.2−100 K, 8 T spectra clearly demonstrates that $D = 15 \pm 5$ cm^{-1}, $E/D \sim 0.1(1)$, $A_x/g_n\beta_n = +5(1)$ T, $A_y/g_n\beta_n = +10(1)$ T, and $A_z/g_n\beta_n = -29(3)$ T. These spectra could be rationalized only by considering two positive, relatively small hyperfine coupling tensor components (Figure S4). This observation reveals that the **A** tensor is dominated by large orbital contributions, vide infra. The ZFS parameters were further corroborated by analysis of the HFEPR spectra and magnetic data (Figures 5 and S1). The simulations presented here were obtained using the numerical values of D, E/D, and g determined from HFEPR and the values of the **A** tensor components (α_{EFG}, β_{EFG}, and γ_{EFG}) and η obtained from the least-squares fitting of selected sets of spectra and spectral simulations of the complete data set (Table 1). Interestingly, this table shows that the spectroscopic behavior of **2** is rather dissimilar from that of other three-coordinate, β-diketiminate-

Table 1. Fine Structure and Hyperfine Structure Parameters of 2 and 3 (bold) and Relevant Complexes

complex	CN	δ (mm/s)	D (cm^{-1})	E/D	ΔE_Q (mm/s)	η	g_x	g_y	g_z	$A_x/g_n\beta_n$ (T)	$A_y/g_n\beta_n$ (T)	$A_z/g_n\beta_n$ (T)
2	3	0.55(1)	+17.4[a]	0.11[a]	−1.48(1)[b]	0.3(1)[b]	2.18[a]	2.32[a]	1.92[a]	+4.8(2)	+9.8(2)	−29(3)
LFeCl[c]		0.74	≤−100[d]	n.a.	−1.61	0.5	n.a.	n.a.	2.72[e]	n.a.	n.a.	+62
$LFeCH_3$[c]		0.48	≤−100[d]	n.a.	+1.74	0.2	n.a.	n.a.	2.85[e]	n.a.	n.a.	+82
$Ph_4P[Fe(SR)_3]\cdot 2MeCN\cdot C_7H_8$[f]		0.56(1)	+10.2(5)	0	−0.83(2)	0	n.a.	n.a.	n.a.	−5.5(4)	−5.5(4)	−21.2(10.2)
$[Li(THF)_2Fe(SR)_3]\cdot{}^1/_2C_6H_{14}$[f]		0.60(1)	+14(3)	0.25	−0.87(2)	0.93(7)[g]	n.a.	n.a.	n.a.	−2.8[g]	+3.3[g]	−26(3)[g]
3	4	0.80(2)	−25(5)	0.15(5)[h]	1.80(2)[i]	1.0[i]	2.0	2.0	2.4	−20(5)	−28(3)	+9.8(2)
$LFe(\mu_2\text{-}Cl)_2Li(THF)_2$[j]		0.90(2)	−14(2)	0.10(4)	2.40(2)	0.75(2)	2.4(2)[j]	2.0	2.0[j]	+2.3/+1.0[j,k]	−21.5	−21.5[j]

[a]Values determined from analysis of the HFEPR spectra. The unexpectedly lower than $g_e = 2.00$ g_z value might be an experimental artifact due to partial alignment of the microcrystalline powder. [b]The EFG tensor is rotated from the reference frame of the ZFS, as described by the Euler angles $\alpha_{EFG} = 55(3)°$, $\beta_{EFG} = 90(5)°$, and $\gamma_{EFG} = 0(5)°$. [c]Reference 5. [d]Estimated value based on the fact that for all experimental conditions only the ground-state quasi-doublet is thermally populated. This value highlights the presence for these complexes of a nearly complete unquenching of the orbital momentum and the failure, in this case, of the quadratic spin Hamiltonian described by eq 1. [e]Intrinsic $S = 2$ value calculated using the $g_{effective} = 4g_z$ formula from the experimentally observed effective g values, that is, $g_{effective}(LFeCl) = 10.9(5)$ and $g_{effective}(LFeCH_3) = 11.4(1)$, respectively. [f]Reference 35. R = C_6H_2-2,4,6-t-Bu_3. [g]The EFG tensor is rotated from the reference frame defined by the ZFS tensor by $\alpha_{EFG} = 40°$ and $\beta_{EFG} = \gamma_{EFG} = 0°$. The hyperfine splitting tensor **A** is rotated from the reference frame of the ZFS by $\alpha_A = 60°$ and $\beta_A = \gamma_A = 0°$. [h]Our simulations of the 4.2 K spectra suggest that this parameter is distributed. For Figure 4, the calculated 4.2 K, 0.5 T spectrum was obtained using $E/D = 0.1$, 4.2 K, 4.0 T using $E/D = 0.15$, and 4.2 K, 8.0 T using $E/D = 0.2$. All other spectra of Figures 4 and S6 were simulated using $E/D = 0.15$. [i]The EFG tensor is rotated from the reference frame of the ZFS, as described by the Euler angles $\alpha_{EFG} = 0°$, $\beta_{EFG} = 10(5)°$, and $\gamma_{EFG} = 0°$. [j]Reference 33. These values were obtained using a spin Hamiltonian that, unlike eq 1, is quantized along x. Therefore, to compare the values of the **A** and **g** tensor components with those of **2** and **3**, switch x with z. [k]These values represent the centers of a Gaussian distribution with a line width at half-maximum of 2.0 T.

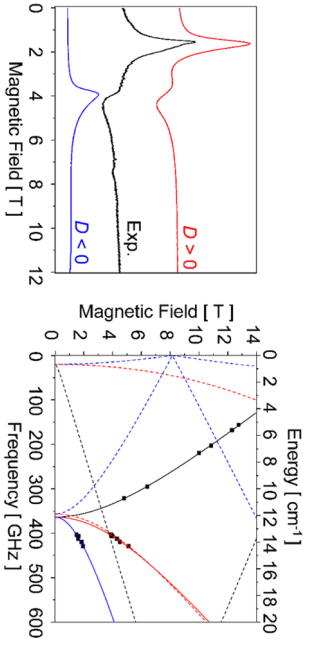

Figure 5. Left: HFEPR spectrum recorded for **2** at 5 K, 406.4 GHz (black trace). The red and blue traces are powder-pattern simulations obtained for $S = 2$ assuming a positive and negative, respectively, ZFS parameter D where $|D| = 17.4$ cm^{-1}, $E/D = 0.11$, $g_x = 2.18$, $g_y = 2.32$, and $g_z = 1.92$. Right: Field versus frequency dependence of the observed resonances indicated as black squares. The curves are simulations using spin-Hamiltonian parameters as above. Red curves represent turning points with the magnetic field B_0 parallel to the x axis of the ZFS tensor. Blue: $B_0 \| y$. Black: $B_0 \| z$. The solid curves are dependencies predicted for the resonances originating from the ground-state spin sublevel ($M_S = 0$), and the dotted lines are obtained for those originating from excited-state M_S levels.

supported iron(II) complexes. In contrast, the electronic structure of **2** is comparable to that of a distorted three-coordinate, homoleptic, sulfido-supported iron(II) complex.

Inspection of Figures 4 (right) and S7 shows that for **3** at 4.2 K the applied field leads to a hyperfine splitting pattern that is remarkably different from that observed for **2**. Thus, even a relatively small field of 0.5 T induces a fully developed magnetic hyperfine splitting. This behavior reveals a ground state consisting of a nearly degenerate quasi-doublet of spin-orbital sublevels. Thus, the ZFS of the two lowest spin sublevels is readily overwhelmed by the applied field through the Zeeman interaction. In turn, this observation strongly supports the presence of a negative ZFS parameter D for **3** (see the Supporting Information). This suggestion is validated by our spectral simulations, which reveal that, indeed, $D = -25(5)$ cm^{-1}. Moreover, we find that the $A_z/g_n\beta_n = +9.8(2)$ tensor component dominates the field-dependent spectra recorded at 4.2 K. Our simulations also suggest that the fine structure parameter E/D is distributed (see the Supporting Information). This behavior is reminiscent of that observed for the four-coordinate $LFe(\mu_2\text{-}Cl)_2Li(THF)_2$ complex (Table 1). The ZFS parameters were further corroborated by analysis of the magnetic susceptibility and of the reduced magnetization data (Figure S2).

3.5. HFEPR. HFEPR experiments on complex **2** resulted in fairly strong spectra in the frequency range of 146−406 GHz at liquid-helium temperatures (Figure 5). The spectra could be effectively interpreted as originating from an $S = 2$ species characterized by a positive ZFS parameter $D = 17.4$ cm^{-1} and sizable rhombicity of the ZFS tensor, $E/D = 0.11$.

HFEPR experiments on complex **3** in the same conditions as those for **2** yielded no spectra, with the exception of weak resonances that could be attributed to iron(III) impurity/impurities (not shown). This is easy to understand in the case of large negative D. In the latter case, the energy splitting between the populated ground-state quasi-doublet of $|S, m_S\rangle \approx |2, \pm 2\rangle$ states and the higher-lying $|2, \pm 1\rangle$ states, on the order of $3|D| \sim 75$ cm^{-1} (according to the Mössbauer results), is much too large to be coupled even by the highest available subterahertz wave frequency and magnetic field.

4. DISCUSSION

4.1. Stereochemistry and Electronic Structure of the $R_2PPSiMe_3^-$ Anions. The phosphanylphosphido anions are a relatively new class of ligands. They coordinate metal ions in a chelating or nonchelating fashion by adopting either a synclinal or an anticlinal conformation (Schemes S1 and S2). In particular, inspection of Figures 1 and 2 shows that the coordination numbers and geometries of the iron(II) sites of **2** and **3** are essentially determined by the conformations of the $R_2PPSiMe_3$ ligands. The electronic structures of these ligands are virtually unexplored. To assess the steric and electronic factors responsible for their versatility, we have performed a series of DFT calculations at the B3LYP/6-311G, B3LYP/6-311++G*, and BPW91/ccc-pvtz levels of theory. For a detailed discussion, see the Supporting Information.

We have explored the stereochemistry of the $R_2PPSiMe_3^-$ ligands by scanning the potential energy surfaces (PESs) of selected $R_2PPSiMe_3^-$ anions, as well as of H_2PPH^- along the ∠(CPPSi) dihedral angle or ∠(HPPH) dihedral angle in the case of H_2PPH^- (Figures 6 and S11). For the putative H_2PPH^-

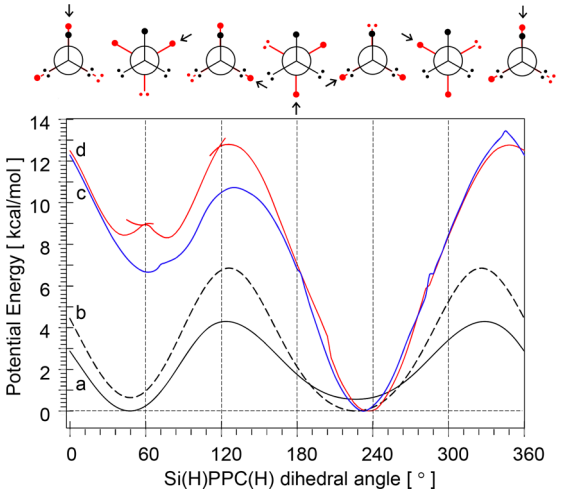

Figure 6. Dependence of the ground-state PES on the Si(H)PPC(H) dihedral angle calculated at the BPW91/cc-pvtz level of theory for the H_2PPH^- (a), $H_2PPSiH_3^-$ (b), *i*-$Pr_2PPSiMe_3^-$ (c), and *t*-$Bu_2PPSiMe_3^-$ (d) anions. The Newman projection diagrams shown above the graph, drawn along the P−P bond, indicate the conformations corresponding to the particular values of the dihedral angles (highlighted by the black arrow).

and $H_2PPSiH_3^-$ anions, which lack bulky substituents, the predicted minima corresponding to the approximate synclinal and anticlinal conformations are nearly degenerate and their relative energies are found to be within 0.5 kcal/mol from each other. However, for the remaining anions, while the $SiMe_3$ substituent of the phosphido group is kept constant, the synclinal conformer is destabilized by an increase in the size of the phosphanyl substituents (Figure S11, left). The difference in the relative energies increases roughly proportionally with the increasing size of the substituents (R = H, Me, *i*-Pr, *t*-Bu); $d(\Delta E)/dV = 0.075(5)$ kJ/mol·Å^3. Thus, for *i*-$Pr_2PPSiMe_3^-$, the synclinal conformer is ∼6.5 kcal/mol higher in energy than the anticlinal conformer. For *t*-$Bu_2PPSiMe_3^-$, this energy difference increases to ∼8.0 kcal/mol. Concomitantly, the increase in the size of the substituents leads to a more complicated PES reflected by the presence of ltwo ocal minima for the synclinal conformer of *t*-$Bu_2PPSiMe_3^-$ and several discontinuities for the PES of *i*-$Pr_2PPSiMe_3^-$ (Figure S11, right).

The electronic structures of the phosphanylphosphido anions were monitored by performing for each minimum an analysis of the natural bond orbitals (NBOs) and canonical molecular orbitals (see the Supporting Information. Thus, we found that (i) the ground-state electronic configurations are minimally affected by the conformational change (Tables S5 and S6), (ii) two of the three phosphorus lone pairs are accommodated by hybrid sp^2/sp^3 orbitals, while the other is supported by a nonbonding P_{Si}-localized p_y orbital (Figure S12), (iii) the negative charge is localized mainly on the phosphido moiety, and (iv) the P−P bond is stabilized by non-Lewis-type, donor−acceptor interactions involving the empty low-lying, phosphorus-based d orbitals (Figure S13). Thus, the X-ray crystallographic investigations of various chemical species that enclose a phosphanylphosphido moiety including **2** and **3** revealed a fairly consistent P−P bond length of 2.16 ± 0.2 Å. This value is somewhat shorter than that of a typical single P−P bond, that is, 2.20 Å.[52,53] This observation led to the inference that for these ligands the P−P bond exhibits multiple-bond character.[36] Our calculations support these arguments; we obtained a Wiberg bond index of the P−P interaction ranging from 1.03 to 1.17 (Table S3). This finding is further corroborated by the natural resonance theory, which yielded a natural bond order of the P−P bond of 1.05(4), as well as the predicted weights of the dominant resonance structures (Table S4 and Schemes S1 and S2).[54]

4.2. Ground-State Geometries and Electronic Configurations of 2 and 3. Complexes **2** and **3** are differentiated from one another by the coordination number of the metal ion that is imposed by the conformation adopted by the phosphanylphosphido ligand. For **2**, the phosphanylphosphido ligand adopts an anticlinal conformation, which leads to a monodentate binding mode. For **3**, the phosphanylphosphido adopts a synclinal conformation, which, in turn, allows for a bidentate, chelating mode. Considering that the synclinal conformation is destabilized by intraligand steric interactions, the latter observation indicates that the higher-energy conformation of the secondary ligand and the higher coordination number of **3** are stabilized by a strong chelating effect. Moreover, compared to most of the other previously characterized *β*-diketiminate-supported iron(II) complexes, the geometries of **2** and **3** are differentiated by the fact that the iron ion is located out-of-the-plane of the diketiminate ligand. This distinctive structural feature is induced, specifically, by the shape asymmetry of the phosphanylphosphido anions, which leads to an increased anisotropy in the steric repulsions among the two iron-bound ligands (Figures S14−S16).

Each geometry optimization of **2** and **3** was followed by time-dependent DFT (TDDFT) calculations. The observation of only positive excitation energies allowed us to establish the presence of an electronic ground state. The character of the electronic configuration was assessed on the basis of the Mulliken population analysis and NPA. Compared to the Mulliken population analysis, NPA provides a more unified picture of the electron distributions of **2** and **3**, which are less strongly dependent on the choice of the computational method (Tables S11−S14). Consequently, in our analysis of the electronic structure, we focused on the results provided by NPA. We found that for **2** the $3d_{z^2}$ orbital is essentially doubly occupied so that, in a first approximation, the electronic configuration of the formal iron(II) ion can be described using

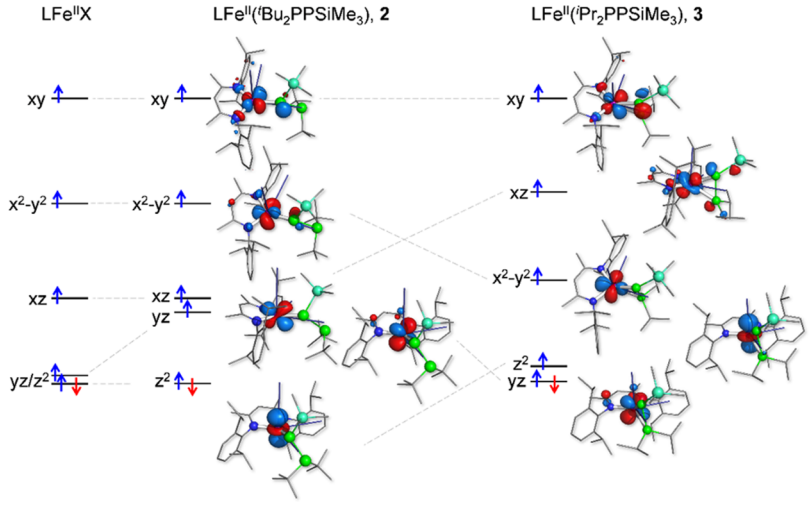

Figure 7. Crystal-field-splitting diagram of the iron 3d orbitals of **2** and **3** derived from analysis of the TDDFT calculations performed using the BPW91/cc-pvtz functional/basis set combination (Table S7). The coordinate system was selected such that the *z* axis is perpendicular to the N−Fe−N plane and FeP_{Si} is contained in the *xz* plane. For comparison, we have also included the crystal-field-splitting diagram of the previously investigated three-coordinate LFe^{II}X complexes.

the $|(z^2)^2(x^2 - y^2)^\alpha(xy)^\alpha(xz)^\alpha(yz)^\alpha|$ Slater determinant. The ground-state electronic configuration of **3** exhibits a doubly occupied $3d_{yz}$ orbital and thus, to a good degree, can be approximated as $|(z^2)^\alpha(x^2 - y^2)^\alpha(xy)^\alpha(xz)^\alpha(yz)^2|$. However, we find that the iron sites of **2** (**3**) have an increased low-valent character. Accordingly, up to 0.8 (0.9), additional electrons are donated from the two ligands to the iron mainly into the empty 4s, β-$3d_{x^2-y^2}$, and β-$3d_{xy}$($3d_{xz}$) iron orbitals; for details, see the Supporting Information discussion and Tables S8−S14.

4.3. Excited Orbital States and ZFS Parameters of 2 and 3. Analysis of the TDDFT results shows that the lowest-energy one-electron excitations correspond to d−d transitions (Table S7). Consequently, these calculations allow us to build up the crystal-field-splitting diagram of **2** and **3** (Figure 7). For comparison, this figure also includes the crystal-field splitting of LFe^{II}X (X = CH_3^-, Cl^-, NHTol$^-$, NH*t*-Bu$^-$), the series of β-diketiminate iron(II) complexes that were investigated by Andres et al.[5] In this case, the most important feature of the crystal-field splitting is given by the near-degeneracy of the $\{3d_{z^2}/3d_{yz}\}$ orbitals. The spin−orbit coupling of the two lowest configurations derived from the highest spin-down, β electron being placed either in a $3d_{z^2}$ or in a $3d_{yz}$ orbital leads to unquenching of the angular orbital momentum along the *x* direction ($\langle\hat{L}_x\rangle \sim \pm\sqrt{3}$), that is, along the Fe−X bond. Ultimately, this interaction yields a ground state consisting of a magnetically uniaxial spin-orbital quasi-doublet that is quantized along the *x* direction, where $g_{eff,x} \gtrsim 10$ and $g_{eff,y} \approx g_{eff,z} \approx 0.1$. The ground-state quasi-doublet is virtually isolated from the lowest excited states. Although not applicable (with the spin−orbit interaction being treated as a perturbation of the crystal-field splitting), in the framework of a quadratic $S = 2$ spin Hamiltonian, the ground-state quasi-doublet of LFe^{II}X would correspond to the $|S, m_s\rangle \approx |2, \pm2\rangle$ spin sublevels. Moreover, the ZFS parameter *D* is unusually large so that, instead of having a value of only a few wavenumbers, $|D| \sim \lambda$, where $\lambda \approx -100$ cm^{-1} is the spin−orbit coupling constant of the iron(II) ions.

Considering that the metal sites of LFe^{II}X and LFe^{II}(*t*-Bu_2PPSiMe$_3$) have identical coordination numbers and similar geometries, we expected them to have comparable magnetic properties and ground-state electronic configurations. However, the spectroscopic characterization of **2** revealed a magnetic behavior that is dramatically different from that of the LFe^{II}X complexes. Thus, **2** exhibits a quintet ground spin state with a positive ZFS parameter, $D = +17.4$ cm^{-1}, so that the lowest spin sublevel corresponds to $|S, m_S\rangle \cong |2, 0\rangle$. Inspection of Figure 7 reveals the origin of this surprising difference: the interaction of the metal center with the *t*-Bu_2PPSiMe$_3$ ligand, in particular with the $SiMe_3$ group, leads to destabilization of the $3d_{yz}$ orbital by an energy that is of the same magnitude as that of the $3d_{xz}$ orbital. Consequently, for **2** we have an isolated $3d_{z^2}$-type state separated by ∼2600−3200 cm^{-1} from the two lowest excited-state orbitals, $3d_{yz}/3d_{xz}$. Interestingly, the DFT-predicted crystal-field diagram of **2** is analogous to that inferred for the homoleptic, three-coordinate, planar $[Fe^{II}(SR)_3]^-$ (R = C_6H_2-2,4,6-*t*-Bu_3) complexes described by Power and co-workers.[33,34]

The TDDFT-derived orbital-splitting diagram of Figure 7 provides a clear rationale for the puzzling similarity between the fine and hyperfine structures of **2** with those of the iron(II) thiolate complexes, in particular of $[Li(THF)_2Fe(SR)_3$ (Table 1). For the latter complex, the bridging by the Li^+ ion of two *S*-thiolates leads to the lowering of the expected trigonal symmetry such that one of the ∠(SFeS) is 92°. This value is similar to ∠(NFeN) ≈ 94° of **2**. In both cases, the general features of the $S = 2$ ground-state ZFS can be rationalized by treating the spin−orbit interaction, $\hat{H}_{SO} = \lambda\hat{\mathbf{L}}\cdot\hat{\mathbf{S}}$, as a perturbation of the crystal-field splitting. Considering the $3d_{z^2}$ character of the ground state, the important matrix elements are $\langle 3d_{z^2}|\hat{L}_x|3d_{yz}\rangle = -\langle 3d_{z^2}|\hat{L}_y|3d_{xz}\rangle = -i\sqrt{3}$. These show that $\hat{H}_{SO}$ mixes the $3d_{z^2}$ ground state with the two lowest excited states, $\{3d_{xz}/3d_{yz}\}$. The spin−orbit contributions to the ZFS and **g** tensors are $D_x = -3\lambda^2/\varepsilon$ ($3d_{yz}$), $D_y = -3\lambda^2/\varepsilon$ ($3d_{xz}$), and $D_z = 0$ and $g_x = 2.00 - 3\lambda/\varepsilon$ ($3d_{yz}$), $g_y = 2.00 - 3\lambda/\varepsilon$ ($3d_{xz}$), and $g_z = 2.00$, respectively. The experimental $D = +17.4$ cm^{-1} and $E/D = 0.11$ values yield the $D_{XX} = -3.9$ cm^{-1}, $D_{YY} = -7.7$ cm^{-1}, and $D_{ZZ} = +11.6$ cm^{-1} diagonal components of the traceless **D** tensor. In turn, these values were used to determine the magnitude of the spin−orbit coupling along the *x* and *y* directions, $D_x = -15.5$ cm^{-1} and $D_y = -23.2$ cm^{-1}. Using these

values to minimize the perturbation theory expressions $\{15.5\varepsilon(3d_{yz}) - 3\lambda^2 = 0;\ 23.2\varepsilon(3d_{xz}) - 3\lambda^2 = 0;\ 0.18\varepsilon(3d_{yz}) = 3\lambda;\ 0.32\varepsilon(3d_{yz}) = 3\lambda\}$ with respect to $\varepsilon(3d_{yz})$, $\varepsilon(3d_{xz})$ and λ parameters, we obtained $\varepsilon(3d_{yz}) = 1400\ cm^{-1}$, $\varepsilon(3d_{xz}) = 700\ cm^{-1}$, and $\lambda = -80\ cm^{-1}$. Although these energies are smaller than those predicted by TDDFT, they are still within the margin of error associated with this method.[55]

Upon going from **2** to **3**, the conformational change of the coordinated phosphanylphosphido ligand leads not only to an increase in the coordination number but also a dramatic reorganization of the 3d iron orbitals. In particular, the increase in the Fe−Si distance leads to stabilization of the $3d_{yz}$ orbital by such a degree that it becomes even lower in energy than the $3d_{z^2}$ orbital. Additionally, displacement of the P_{Si} biting atom from the N−Fe−N plane leads to stabilization of the $3d_{x^2-y^2}$ and destabilization of the $3d_{xz}$ orbitals such that when compared to **2** and the $LFe^{II}X$ complexes, their order is reversed. Although the latter orbital is also destabilized by the bonding interaction of the metal ion with P_C, its energy is still lower than that of $3d_{xy}$. Similar to the electronic structures of $[LFe^{II}X]$ and $[LFe(\mu_2\text{-}Cl)_2Li(THF)_2]$ (Table 1), the most important feature of the crystal-field-splitting diagram of **3** is given by the low-energy separation of the two lowest orbitals, that is, $\varepsilon(3d_{z^2})$. Thus, the magnetic properties of **3** are dominated by the mixing of the two lowest states by the two lowest orbital states. Thus, perturbation theory yields $D = D_x \approx -3\lambda^2/\varepsilon(3d_{z^2})$ and $\Delta g_x = g_x - 2.00 \approx -6\lambda/\varepsilon(3d_{z^2})$. Consequently, the easy axis of magnetization of **3**, that is, the quantization axis of the spin operator $\hat{\mathbf{S}}$ (z axis of eq 1) is contained by the N−Fe−N and P−Fe−P planes being found, roughly, along the Fe−P_{Si} bond. Using the $D = -25\ cm^{-1}$ and $g_z = 2.4$ values derived from field-dependent Mössbauer spectroscopy, no EPR signal was observed for **3**, and we obtain a coarse estimate of $\lambda = -125\ cm^{-1}$ and $\varepsilon(3d_{z^2}) = 1875\ cm^{-1}$. The latter value is in good agreement with the TDDFT-predicted energy of the lowest $3d_{z^2}$-type orbital state.

4.4. Hyperfine Structure Parameters of 2 and 3. Interestingly, both the isomer shift and quadrupole splitting values of **2** are lower than those expected for a typical high-spin iron(II) site ($\delta \geq 0.6$ mm/s and $|\Delta E_Q| \geq 1.5$ mm/s), vide infra. However, the observed isomer shift value is similar to not only that of $[Fe^{II}(SR)_3]^-$ complexes, $\delta = 0.55-0.60$ mm/s, but also those observed for the analogous three-coordinate iron(II) sites supported by β-diketiminate complexes that exhibit a $3d_{z^2}$ ground state, i.e., $LFe^{II}(\mu_2\text{-}N_2^{2-})Fe^{II}L$ ($\delta = 0.62$ mm/s) and $LFe^{II}CH_3$ ($\delta = 0.48$ mm/s).[56] Consequently, these observations disclose that the lower than usual δ value of **2** originates from the combined effects of a low coordination number and of the symmetry-allowed mixing of $3d_{z^2}$ and 4s atomic orbitals (Table S13). The increased population of the 4s atomic orbital, due to the formation of a hybrid $3d_{z^2}$−4s orbital, leads to a higher electronic density at the nucleus and thus to a lower value of δ. At the B3LYP/6311G level of theory, the isomer shift values predicted for **2**, $\delta_{calc} = 0.46$ mm/s and $\delta_{exp} = 0.55$ mm/s, and **3**, $\delta_{calc} = 0.69$ mm/s and $\delta_{exp} = 0.80$ mm/s, are within the error associated with this method (~0.15 mm/s).

The fine structure of **2** fits well with a $3d_{z^2}$-type ground-state configuration. For such a state, we expected the largest principal component of the EFG to be negative and to be aligned with the z axis (see the Supporting Information). However, we found that the experimental EFG tensor exhibits a small positive component along the z axis. Analysis of the DFT-predicted EFG tensors shows that for **2** the individual components of the valence and ligand contributions, including the largest components, are virtually collinear and have opposite signs. Consequently, their sums lead to an overall EFG tensor with components of diminished magnitude for which the largest negative component is parallel, rather than perpendicular, to the N−Fe−N plane. Interestingly, an analogous large V_{ligand} is also responsible for the nearly quenched quadrupole splitting of square-planar iron(II) complexes ($\Delta E_Q = 0.55$ mm/s),[57] the large $\Delta E_Q = +1$ to $+2$ mm/s value of some iron(III) porphyrins,[58] and the $\Delta E_Q = +5.12$ mm/s value of $Fe^{III}[N(SiMe_3)_2]_3$.[59] For high-spin iron(III) compounds, the ^6S character of the ground-state configuration is expected to lead, in an ideal case, to a zero $V_{valence}$ contribution. For **3**, the doubly occupied $3d_{yz}$ orbital leads to a nearly axial $V_{valence}$ for which the large positive component, $V_{valence,max} \cong +3$ mm/s, is found along the easy axis of magnetization, that is, approximatively along the Fe−P_{Si} bond. Similar to **2**, the approximate planar arrangement of the ligands with increased negative charges of **3** leads to a large V_{ligand} contribution for which the largest positive component is essentially orthogonal to the N−Fe−N plane. Together, these contributions lead to a rhombic, $\eta \sim 1$ EFG tensor that exhibits a large positive along the easy axis of magnetization (found approximately along the Fe−P_{Si} bond), a large negative component roughly orthogonal to the β-diketiminate plane, and a null component normal to the P−Fe−P plane (Table S15).

The magnetic hyperfine splittings of **2** and **3** are described using the hyperfine coupling tensor **A**, which results from the interplay of three distinct interactions $A_\xi = A_{FC,\xi} + A_{SD,\xi} + A_{L,\xi}$. The individual components represent the Fermi contact term ($A_{FC,\xi} = -\kappa P$), the spin dipolar contribution ($A_{SD,\xi} = l_\xi P$), and the orbital term ($A_{L,\xi} = \Delta g_\xi P$). The $P = g_e g_n \beta_e \beta_n \langle r^{-3} \rangle_{3d}$ scaling factor of the magnetic hyperfine interaction can be conveniently expressed in magnetic field units (Tesla) by taking the ratio $P/g_n\beta_n$. On the basis of Hartree−Fock solutions for the radial 3d functions, P was estimated at about 64 T for high-spin ferrous ions. Inspection of Table 1 shows that for **2** $\Delta g_x = 0.18$, $\Delta g_y = 0.32$, and $\Delta g_z = 0.00$ (assuming that the lower than 2.00 value of g_z is an experimental artifact). Moreover, the $3d_{z^2}$ ground-state configuration leads to the $l_{x,y} = {}^1/_{14}$ and $l_z = -{}^1/_7$ factors of the spin dipolar contribution. By introducing these values into the expressions of the hyperfine coupling tensor components and solving for κ and P, we obtain for **2** a covalently reduced value of $P = 35$ T, $\kappa = 0.68$, and a Fermi contact term $A_{FC} = -23$ T. Albeit, the P value is much smaller than that of the free ion and it is very similar to that observed for $Ph_4P[Fe(SR)_3]$, that is, $P = 38.7$ T. For **3**, $\Delta g_x = 0.4$ along the easy axis of magnetization (z axis of the spin Hamiltonian) and $\Delta g_{y,z} = 0.0$, together with the $l_x = {}^1/_7$ and $l_{z,y} = -{}^1/_{14}$ factors, lead us to $P = 55$ T, $\kappa = 0.36$, and a Fermi contact term $A_{FC} = -20$ T.

5. CONCLUSIONS

When the lithiated diphosphanes $R_2PP(SiMe_3)Li$ (R = *t*-Bu, *i*-Pr) were reacted with $[LFeCl_2Li(DME)_2]$ (L = Dippnacnac), they furnished two novel phosphanylphosphido complexes of iron(II). Their structural characterization revealed that while, for **2**, $R_2PPSiMe_3^-$ adopts an end-on coordination for **3**, the P_2-containing moiety adopts an side-on coordination. Interestingly, the reaction of $(i\text{-}Pr_2N)_2PP(SiMe_3)Li$ with $[LFeCl_2Li(DME)_2]$ is considerably more complex and yields not another iron(II) complex but **4**. The electronic structures of **2** and **3** were characterized using magnetometry, field-dependent ^{57}Fe

Mössbauer spectroscopy, and HFEPR. This investigation revealed that **2** and **3** exhibit distinct magnetic properties and electronic structures. Thus, for **2**, the lowest spin sublevel is given by a $|S, m_S\rangle = |2, 0\rangle$ substate. In contrast, the ground state of **3** consists of an isolated quasi-doublet with a $|S, m_S\rangle \sim |2, \pm 2\rangle$ parentage. Our DFT calculations provide a clear rationale for the observed fine and hyperfine structure parameters. For example, **2** exhibits a ground state for which z^2 is doubly occupied. Moreover, its ZFS originates from the strong spin−orbit coupling of the ground state with two low-lying orbital states provided by the $\{z^2 \rightarrow xz\}$ and $\{z^2 \rightarrow yz\}$ β-electron excitations. For **3**, the high-spin iron(II) site adopts a ground-state electronic configuration for which the yz orbital is doubly occupied. In this case, the observed ZFS of the spin ground state originates from the spin−orbit interaction acting on the two configurations spanned by the $\{yz \rightarrow z^2\}$ excitation of the single β-3d electron.

Crystallographic data for the structures of **2**−**4** reported in this paper have been deposited with the Cambridge Crystallographic Data Centre as supplementary publications CCDC 1053578, 1053579, and 1053580.

■ ACKNOWLEDGMENTS

J.P., R.G., and Ł.P. thank the National Science Centre NCN (Grant 2012/06/M/ST5/00472) for financial support. A portion of this work was performed at the National High Magnetic Field Laboratory, which is supported by National Science Foundation Cooperative Agreement No. DMR-1157490 and the State of Florida. S.A.S. acknowledges partial support from the Jack E. Crow postdoctoral fellowship. The Mössbauer instrument was purchased using the NHFML User Collaboration Grant Program (UCGP-5064) awarded to Dr. Andrzej Ozarowski. A.D.-A. acknowledges partial support from the NSF (Grant CHE-1152020). The authors thank A. Ozarowski for his EPR simulation and fitting program *SPIN*. Moreover, the authors thank Karlsruhe Nano Micro Facility, Karlsruhe Institute of Technology, for X-ray diffraction measurements.

■ REFERENCES

(1) Holland, P. L. Electronic Structure and Reactivity of Three-Coordinate Iron Complexes. *Acc. Chem. Res.* **2008**, *41*, 905−914.
(2) Holland, P. L. Low Coordinate Iron Complexes as Synthetic Models of Nitrogenase. *Can. J. Chem.* **2005**, *83*, 296−301.
(3) Eckert, N. A.; Smith, J. M.; Lachicotte, R. L.; Holland, P. L. Low-Coordinate Fe(II) Amido Complexes of β-Diketiminates: Synthesis, Structure and Reactivity. *Inorg. Chem.* **2004**, *43*, 3306−3321.
(4) Bourget-Merle, L.; Lappert, M. F.; Severn, J. R. The Chemistry of β-Diketiminatometal Complexes. *Chem. Rev.* **2002**, *102*, 3031−3066.
(5) Andres, H.; Bominaar, E. L.; Smith, J. M.; Eckert, N. A.; Holland, P. L.; Münck, E. Planar Three-Coordinate High-Spin Fe(II) Complexes with Large Orbital Angular Momentum: Mössbauer, Electron Paramagnetic Resonance, and Electronic Structure Studies. *J. Am. Chem. Soc.* **2002**, *124*, 3012−3025.
(6) Freedman, D. E.; Harman, W. H.; Harris, T. D.; Long, G. J.; Chang, C. J.; Long, J. R. Slow Magnetic Relaxation in a High-Spin Iron(II) Complex. *J. Am. Chem. Soc.* **2010**, *132*, 1224−1225.
(7) Buhro, W. E.; Chisholm, M. H.; Folting, K.; Huffman, J. C.; Martin, J. D.; Streib, W. E. The Tungsten-Tungsten Triple Bond. 17. Mixed Amido-Phosphido Compounds of Formula $M_2(PR_2)_2(NMe_2)_4$. Comparisons of Amido and Phosphido Ligation and Bridged and Unbridged Isomers. *J. Am. Chem. Soc.* **1992**, *114*, 557−570.
(8) Goel, S. C.; Chiang, M. Y.; Rauscher, D. J.; Buhro, W. E. Comparing the Properties of Homologous Phosphido and Amido Complexes: Synthesis and Characterization of the Disilylphosphido Complexes $\{M[P(SiMe_3)_2]_2\}_2$ where M = Zn, Cd, Hg, Sn, Pb and Mn. *J. Am. Chem. Soc.* **1993**, *115*, 160−169.
(9) Matchett, M. A.; Chiang, M. Y.; Buhro, W. E. Disilylphosphido Complexes $M[P(SiPh_3)_2]_2$, Where M = Zn, Cd, Hg, and Sn: Effective Steric Equivalency of $P(SiPh_3)_2$ and $N(SiMe_3)_2$ Ligands. *Inorg. Chem.* **1994**, *33*, 1109−1114.
(10) Schäfer, H. Übergangsmetallphosphidokomplexe. IV. Phosphido- und Bistrimethylsilylphosphidokomplexe des Eisens. *Z. Anorg. Allg. Chem.* **1980**, *467*, 105−122.
(11) Dobbie, R. C.; Mason, P. R. Reactions of a Terminal Phosphido-Group in an Organo-Iron Complex. Part I. Some Oxygen, Sulphur, and Selenium Derivatives. *J. Chem. Soc., Dalton Trans.* **1973**, 1124−1128.
(12) Lorenz, J.-P.; Pohl, W.; Nöth, H.; Schmidt, H. *P*-Funktionalisierte Diferriophosphonium Salze des Typs $[\{CpFe(CO)_2\}_2PPhR]^+X^-$ und $[\{CpFe(CO)_2\}_2PClR]^+X^-$. *J. Organomet. Chem.* **1994**, *475*, 211−221.
(13) Jones, R. A.; Stuart, A. L.; Atwood, J. L.; Hunter, W. E.; Rogers, R. D. Steric Effects of Phosphido Ligands. Synthesis and Crystal Structure of Di-*tert*-butylphosphido-Bridged Dinuclear Metal-Metal Bonded Complexes of Fe(II), Co(I, II) and Ni(I). *Organometallics* **1982**, *1*, 1721−1723.
(14) Smith, J. M.; Sadique, A. R.; Cundari, T. R.; Rodgers, K. R.; Lukat-Rodgers, G.; Lachicotte, R. J.; Flaschenriem, C. J.; Vela, J.; Holland, P. L. Studies of Low-Coordinate Iron Dinitrogen Complexes. *J. Am. Chem. Soc.* **2006**, *128*, 756−769.
(15) Bai, G.; Wei, P.; Das, A. K.; Stephan, D. W. P−H and P−P Bond Activation by Ni(I) and Fe(I) β-Diketiminato-Complexes. *Dalton Trans.* **2006**, 1141−1146.
(16) Yao, S.; Szilvási, T.; Lindenmaier, N.; Xiong, Y.; Inoue, S.; Adelhardt, M.; Sutter, J.; Meyer, K.; Driess, M. Reductive Cleavage of P_4 by Iron(I) Centres: Synthesis and Structural Characterization of $Fe_2(P_2)_2$ Complexes with Two Bridging P_2^{2-} Ligands. *Chem. Commun.* **2015**, *51*, 6153−6156.

(17) Spitzer, F.; Graßl, C.; Balázs, G.; Zolnhofer, E. M.; Meyer, K.; Scheer, M. Influence of the nacnac Ligand in Iron(I)-Mediated P_4 Transformations. *Angew. Chem., Int. Ed.* **2016**, *55*, 4340−4344.
(18) King, A. K.; Buchard, A.; Mahon, M. F.; Webster, R. L. Facile, Catalytic Dehydrocoupling of Phosphines Using *β*- Diketiminate Iron(II) Complexes. *Chem. - Eur. J.* **2015**, *21*, 15960−15963.
(19) Espinal-Viguri, M.; King, A. K.; Lowe, J. P.; Mahon, M. F.; Webster, R. L. Hydrophosphination of Unactivated Alkenes and Alkynes Using Iron(II): Catalysis and Mechanistic Insight. *ACS Catal.* **2016**, *6*, 7892−7897.
(20) Olkowska-Oetzel, J.; Pikies, J. Chemistry of the Phosphinophosphinidene $^{t}Bu_2P$-P, a Novel *π*-electron Ligand. *Appl. Organomet. Chem.* **2003**, *17*, 28−35.
(21) Pikies, J.; Baum, E.; Matern, E.; Chojnacki, J.; Grubba, R.; Robaszkiewicz, A. The New Synthetic Entry to Phosphinophosphinidene Complexes. Synthesis and Structural Characterisation of the First Side-on Bonded and the First Terminally Bonded Phosphinophosphinidene Zirconium Complexes: [*μ*-(1,2:2-*η*-$^{t}Bu_2P$═P){Zr(Cl)Cp_2}$_2$] and [{Zr(PPhMe$_2$)Cp_2}(*η*^{1}−P$^{t}Bu_2$)]. *Chem. Commun.* **2004**, 2478−2479.
(22) Grubba, R.; Wiśniewska, A.; Baranowska, K.; Matern, E.; Pikies, J. Syntheses and Structures of the First Terminal Phosphanylphosphido Complex of Hafnium [Cp_2Hf(Cl){*η*^{1}-(Me$_3$Si)P-P(NEt$_2$)$_2$}] and the First Zirconocene-Phosphanylphosphinidene Dimer [Cp_2Zr{*μ*$_2$-P-P(NEt$_2$)$_2$}$_2$ZrCp_2]. *Dalton Trans.* **2011**, *40*, 2017−2024.
(23) Grubba, R.; Wiśniewska, A.; Baranowska, K.; Matern, E.; Pikies, J. General Route for the Synthesis of Terminal Phosphanylphosphido Complexes of Zr(IV) and Hf(IV). Structural Investigations of the First Zirconium Complex with a Phosphanylphosphido Ligand. *Polyhedron* **2011**, *30*, 1238−1243.
(24) Grubba, R.; Baranowska, K.; Gudat, D.; Pikies, J. Reactions of Lithiated Diphosphanes R_2P−P(SiMe$_3$)Li (R = ^{t}Bu, ^{i}Pr, $^{i}Pr_2$N, Et$_2$N) with [Cp_2WCl_2]. Syntheses and Structures of the First Terminal Phosphanylphosphido Complexes of Tungsten(IV). *Organometallics* **2011**, *30*, 6655−6660.
(25) Kruczyński, T.; Grubba, R.; Baranowska, K.; Pikies, J. Syntheses and Structures of the First Terminal Phosphanylphosphido Complexes of Molybdenum(IV). *Polyhedron* **2012**, *39*, 25−30.
(26) Zauliczny, M.; Grubba, R.; Ponikiewski, Ł.; Pikies, J. Phosphanylphosphido and Phosphanylphosphinidene Complexes of Zirconium(IV) Supported by Bidentate *N,N* ligands. *Polyhedron* **2017**, *123*, 353−360.
(27) Ponikiewski, Ł.; Ziółkowska, A.; Pikies, J. Reactions of Lithiated Diphosphanes R_2P−P(SiMe$_3$)Li (R = *t*Bu and *i*Pr) with [^{Me}NacnacTiCl$_2$·THF] and [^{Me}NacnacTiCl$_3$]. Formation and Structure of Titanium^{III} and Titanium^{IV} *β*-Diketiminato Complexes Bearing the Side-on Phosphanylphosphido and Phosphanylphosphinidene Functionalities. *Inorg. Chem.* **2017**, *56*, 1094−1103.
(28) Domańska-Babul, W.; Chojnacki, J.; Matern, E.; Pikies, J. Reactions of R_2P-P(SiMe$_3$)Li with [(R′$_3$P)$_2$PtCl$_2$]. A General and Efficient Entrance to Phosphanylphosphinidene Complexes of Platinum. Syntheses and Structures of [(*η*$_2$-P═P$^{i}Pr_2$)Pt(p-Tol$_3$P)$_2$], [(*η*$_2$-P═P$^{t}Bu_2$)Pt(p-Tol$_3$P)$_2$], [{*η*$_2$-P═P(N$^{i}Pr_2$)2}Pt(p-Tol$_3$P)$_2$] and [{(Et$_2$PhP)$_2$Pt}$_2$P$_2$]. *Dalton Trans.* **2009**, 146−151.
(29) Grubba, R.; Baranowska, K.; Chojnacki, J.; Pikies, J. Access to Side-On Bonded Tungsten Phosphanylphosphinidene Complexes. *Eur. J. Inorg. Chem.* **2012**, *20*, 3263−3265.
(30) Grubba, R.; Ordyszewska, A.; Kaniewska, K.; Ponikiewski, Ł.; Chojnacki, J.; Gudat, D.; Pikies, J. Reactivity of Phosphanylphosphinidene Complex of Tungsten(VI) toward Phosphines: A New Method of Synthesis of *catena*-Polyphosphorus Ligands. *Inorg. Chem.* **2015**, *54*, 8380−8387.
(31) Grubba, R.; Ordyszewska, A.; Ponikiewski, Ł.; Gudat, D.; Pikies, J. An Investigation on the Chemistry of R_2P═P Ligand: Reactions of Phosphanylphosphinidene Complex of Tungsten(VI) with Electrophilic Reagents. *Dalton Trans.* **2016**, *45*, 2172−2179.
(32) Krautscheid, H.; Matern, E.; Kovacs, I.; Fritz, G.; Pikies, J. Komplexchemie P-reicher Phosphane und Silylphosphane. XIV. Phosphinophosphiniden $^{t}Bu_2$P-P als Ligand in den Pt-Komplexen [{*η*^{2}-$^{t}Bu_2$P-P}Pt(PPh$_3$)$_2$] und [{ *η*^{2}-$^{t}Bu_2$P-P}Pt(PEtPh$_2$)$_2$]. *Z. Anorg. Allg. Chem.* **1997**, *623*, 1917−1924.
(33) Stoian, S. A.; Smith, J. M.; Holland, P. L.; Münck, E.; Bominaar, E. L. Mössbauer, Electron Paramagnetic Resonance, and Theoretical Study of a High-Spin, Four Coordinate Fe(II) Diketiminate Complex. *Inorg. Chem.* **2008**, *47*, 8687−8695.
(34) MacDonnell, F. M.; Ruhlandt-Senge, K.; Ellison, J. J.; Holm, R. H.; Power, P. P. Sterically Encumebred Iron(II) Thiolate Complexes: Synthesis and Structure of Trigonal Planar [Fe(SR)$_3$]$^{-}$ (R = 2,4,6-*t*-Bu$_3$C$_6$H$_2$) and Mössbauer Spectra of Two and Three-Coordinate Complexes. *Inorg. Chem.* **1995**, *34*, 1815−1822.
(35) Sanakis, Y.; Power, P. P.; Stubna, A.; Münck, E. Mössbauer Study of the Three-Coordinate Planar Fe^{II} [Fe(SR)$_3$]$^{-}$ (R = C$_6$H$_2$-2,4,6-$^{t}Bu_3$): Model for the Trigonal Iron Sites of the MoFe$_7$S$_9$: Homocitrate Cofactor of Nitrogenase. *Inorg. Chem.* **2002**, *41*, 2690−2696.
(36) Domańska-Babul, W.; Baranowska, K.; Grubba, R.; Matern, E.; Pikies, J. Syntheses and Crystal Structures of Lithium Derivatives of Diphosphanes R_2P-P(SiMe$_3$)Li·3L, R = Ph, ^{i}Pr and Pr_2N, L = THF or DME. *Polyhedron* **2007**, *26*, 5491−5496.
(37) Grubba, R.; Ponikiewski, Ł.; Tomorowicz, Ł.; Pikies, J. [*N,N*′-Bis(2,6-diisopropylphenyl)pentane-2,4-diamine(1−)-2*κ*^{2}*N,N*′]-*μ*$_2$-chlorido-1:2*κ*^{2}*Cl:Cl*-chlorido-2*κ*Cl-bis(1,2-dimethoxyethane-1*κ*^{2}*O,O*′)-iron(II)lithium. *Acta Crystallogr.* **2010**, *E66*, m707.
(38) Sheldrick, G. M. A Short History of SHELX. *Acta Crystallogr., Sect. A: Found. Crystallogr.* **2008**, *64*, 112−122.
(39) Münick, E.; Groves, J. L.; Tumolillo, T. A.; Debrunner, P. G. Computer simulations of Mössbauer spectra for an effective spin S = 1/2 Hamiltonian. *Comput. Phys. Commun.* **1973**, *5*, 225−238.
(40) Hassan, A. K.; Pardi, L. A.; Krzystek, J.; Sienkiewicz, A.; Goy, P.; Rohrer, M.; Brunel, L.-C. Ultrawide Band Multifrequency High-Field EMR Technique: A Methodology for Increasing Spectroscopic Information. *J. Magn. Reson.* **2000**, *142*, 300−312.
(41) Bain, G. A.; Berry, J. F. Diamagnetic Corrections and Pascal's Constants. *J. Chem. Educ.* **2008**, *85*, 532−536.
(42) https://cec.mpg.de/1/research/molecular-theory-and-spectroscopy/dr-eckhard-bill/.
(43) Frisch, M. J.; Trucks, G. W.; Schlegel, H. B.; Scuseria, G. E.; Robb, M. A.; Cheeseman, J. R.; Scalmani, G.; Barone, V.; Mennucci, B.; Petersson, G. A.; Nakatsuji, H.; Caricato, M.; Li, X.; Hratchian, H. P.; Izmaylov, A. F.; Bloino, J.; Zheng, G.; Sonnenberg, J. L.; Hada, M.; Ehara, M.; Toyota, K.; Fukuda, R.; Hasegawa, J.; Ishida, M.; Nakajima, T.; Honda, Y.; Kitao, O.; Nakai, H.; Vreven, T.; Montgomery, J. A., Jr.; Peralta, J. E.; Ogliaro, F.; Bearpark, M.; Heyd, J. J.; Brothers, E.; Kudin, K. N.; Staroverov, V. N.; Keith, T.; Kobayashi, R.; Normand, J.; Raghavachari, K.; Rendell, A.; Burant, J. C.; Iyengar, S. S.; Tomasi, J.; Cossi, M.; Rega, N.; Millam, J. M.; Klene, M.; Knox, J. E.; Cross, J. B.; Bakken, V.; Adamo, C.; Jaramillo, J.; Gomperts, R.; Stratmann, R. E.; Yazyev, O.; Austin, A. J.; Cammi, R.; Pomelli, C.; Ochterski, J. W.; Martin, R. L.; Morokuma, K.; Zakrzewski, V. G.; Voth, G. A.; Salvador, P.; Dannenberg, J. J.; Dapprich, S.; Daniels, A. D.; Farkas, O.; Foresman, J. B.; Ortiz, J. V.; Cioslowski, J.; Fox, D. J. *Gaussian09*, revision D.01; Gaussian, Inc.: Wallingford, CT, 2013.
(44) Glendening, E. D.; Badenhoop, J. K.; Reed, A. E.; Carpenter, J. E.; Bohmann, J. A.; Morales, C. M.; Landis, C. R.; Weinhold, F. *NBO6.0*; Theoretical Chemistry Institute, University of Wisconsin, Madison, WI, 2013.
(45) Vrajmasu, V.; Münck, E.; Bominaar, E. L. Density Functional Study of the Electric Hyperfine Interactions and the Redox-Structural Correlations in the Cofactor of Nitrogenase. Analysis of General Trends in ^{57}Fe Isomer Shifts. *Inorg. Chem.* **2003**, *42*, 5974−5988.
(46) Lu, T.; Chen, F. A Multifunctional Wavefunction Analyzer. *J. Comput. Chem.* **2012**, *33*, 580−592.
(47) Weber, L.; Buchwald, S.; Lentz, D.; Preugschat, D.; Stammler, H.-G.; Neumann, B. Transition-Metal-Substituted Diphosphenes. 29. Cycloaddition Reactions of the Diphosphenyl Complex (*η*^{5}-C$_5$Me$_5$)-(CO)$_2$Fe-P═P-Mes* (Mes* = 2, 4, 6-*t*Bu$_3$C$_6$H$_2$) with Hexafluoroacetone. X-ray Structure Analyses of (*η*^{5}-C$_5$Me$_5$)(CO)Fe-P(═

PMes*)OC(CF_3)$_2$C(O) and (η^5-C_5Me_5)(CO)$_2$Fe-P-P(Mes*)OC-(CF_3)$_2$. *Organometallics* **1992**, *11*, 2351−2353.
(48) Wiśniewska, A.; Baranowska, K.; Grubba, R.; Matern, E.; Pikies, J. Reactions of Lithium Salts of Triphosphanes ^{t}Bu$_2$P-PLi-P^{t}Bu$_2$ and ^{t}Bu$_2$P-PLi-P(NEt$_2$)$_2$ with Metal Complexes [(R_3P)$_2$MCl$_2$] (M = Ni, Pd, Pt, R_3P = Et$_3$P, pTol$_3$P, Ph$_2$EtP, ^{i}Pr$_3$P). *Z. Anorg. Allg. Chem.* **2010**, *636*, 1549−1556.
(49) Grubba, R.; Wiśniewska, A.; Ponikiewski, Ł.; Caporali, M.; Peruzzini, M.; Pikies, J. Reactivity of Diimido Complexes of Molybdenum and Tungsten towards Lithium Derivatives of Diphosphanes and Triphosphanes. *Eur. J. Inorg. Chem.* **2014**, *10*, 1811−1817.
(50) Appel, R.; Gudat, D.; Niecke, E.; Nieger, M.; Porz, C.; Westermann, H. Synthese und Struktur aminosubstituierter Tetraphosphetane. *Z. Naturforsch., B: J. Chem. Sci.* **1991**, *46*, 865−883.
(51) (a) Gütlich, P.; Bill, E.; Trautwein, A. X. *Mössbauer Spectroscopy and Transition Metal Chemistry: Fundamentals and Applications*; Springer-Verlag: Berlin, 2011. (b) Greenwood, N. N.; Gibb, T. C. *Mössbauer Spectroscopy*; Chapman and Hall: London, 1971.
(52) von Schnering, H. G.; Hönle, W. Chemistry and Structural Chemistry of Phosphides and Polyphosphides. 48. Bridging Chasms with Polyphosphides. *Chem. Rev.* **1988**, *88*, 243−273.
(53) Dragulescu-Andrasi, A.; Miller, L. Z.; Chen, B.; McQuade, D. T.; Shatruk, M. Facile Conversion of Red Phosphorous into Soluble Polyphosphide Anions by Reaction with Potassium Ethoxide. *Angew. Chem., Int. Ed.* **2016**, *55*, 3904−3908.
(54) (a) Glendening, E. D.; Weinhold, F. Natural Resonance Theory: I. General Formalism. *J. Comput. Chem.* **1998**, *19*, 593−609. (b) Glendening, E. D.; Weinhold, F. Natural Resonance Theory: II. Natural Bond Order and Valency. *J. Comput. Chem.* **1998**, *19*, 610−627. (c) Glendening, E. D.; Badenhoop, J. K.; Weinhold, F. Natural Resonance Theory: III. Chemical Applications. *J. Comput. Chem.* **1998**, *19*, 628−646.
(55) Wiberg, K. B.; Stratmann, R. E.; Frisch, M. J. A Time-Dependent Density Functional Theory Study of the Electronically Excited States of Formaldehyde, Acetaldehyde and Acetone. *Chem. Phys. Lett.* **1998**, *297*, 60−64.
(56) Stoian, S. A.; Vela, J.; Smith, J. M.; Sadique, A. R.; Holland, P. L.; Münck, E.; Bominaar, E. L. Mössbauer and Computational Study of an N_2 − Bridged Diiron Diketiminate Complex: Parallel Alignement of Iron Spins by Direct Antiferromagnetic Exchange with Activated Dinitrogen. *J. Am. Chem. Soc.* **2006**, *128*, 10181−10192 (Table 2 on p 10189).
(57) Pascualini, M. E.; Di Russo, N. V.; Thuijs, A. E.; Ozarowski, A.; Stoian, S. A.; Abboud, K. A.; Christou, G.; Veige, A. S. A High-Spin Square-Planar Fe(II) Complex Stabilized by a Trianionic Pincer-Type Ligand and Conclusive Evidence for Retention of Geometry and Spin State in Solution. *Chem. Sci.* **2015**, *6*, 608−612.
(58) Gismelseed, A.; Bominaar, E. L.; Bill, E.; Trautwein, A. X.; Winkler, H.; Nasri, H.; Doppelt, P.; Mandon, J.; Fischer, J.; Weiss, F. R. Six-Coordinate Quantum-Mechanically Weakly Spin-Mixed (S = 5/2, 3/2) (triflato)aquairon(III) "Picket-Fence" Porphyrin Complex: Synthesis and Structural, Mössbauer, EPR, and Magnetic Characterization. *Inorg. Chem.* **1990**, *29*, 2741−2749.
(59) Fitzsimmons, B. W.; Johnson, C. E. The Mössbauer Spectrum of a Three-Coordinate Compound, tris (hexamethyldisilylaminato) iron(III), Fe[N($SiMe_3$)$_2$]$_3$. *Chem. Phys. Lett.* **1974**, *24*, 422−424.